

國立臺灣大學電機資訊學院電機工程學系

學士班學生論文

Department of Electrical Engineering

College of Electrical Engineering and Computer Science

National Taiwan University

Bachelor's Thesis

微磁學模擬重金屬覆蓋層實現 SOT-MRAM 決定性位  
元切換

Micromagnetic simulations for deterministic switching in  
SOT-MRAM cell with additional heavy metal capping strip

喬冠豪

Kuan-Hao Chiao

指導教授: 吳育任 博士

Advisor: Yu-Renn Wu, Ph.D.

中華民國 112 年 4 月

April, 2023



國立臺灣大學學士班學生學位論文

口試委員會審定書



微磁學模擬重金屬覆蓋層實現 SOT-MRAM 決定  
性位元切換

Micromagnetic simulations for deterministic  
switching in SOT-MRAM cell with additional heavy  
metal capping strip

本論文係喬冠豪君 (B08901184) 在國立臺灣大學電機工程學系完成之學士班學生學位論文，於民國 112 年 4 月 30 日承下列考試委員審查通過及口試及格，特此證明

口試委員：

吳育仁

(指導教授)

吳偉倫

張子瑋

系主任：



# Acknowledgements

This work has already been published in Applied Physics Letters (APL). I would like to express my sincere gratitude to several individuals who have contributed to the successful completion of my Bachelor's thesis. Firstly, I would like to thank my thesis advisor Yu-Renn Wu, for his valuable guidance, unwavering support, and constructive feedback throughout the thesis writing process. Without his help, this project would not have been possible.

Furthermore, I would like to thank my family for their love and support, and for always encouraging me to pursue my academic goals. Their patience, understanding, and motivation were essential in keeping me focused during the long hours of writing and research.

Finally, I would like to acknowledge the participants of this study, who generously gave their time and effort to provide the data needed for this research. Their contributions were invaluable and greatly appreciated.

Once again, thank you to everyone who played a role in the completion of this thesis. Your support and encouragement have been instrumental in my academic journey.



## 摘要

自旋軌道力磁性隨機存取記憶體 (SOT-MRAM) 近來在記憶體行業中受到廣泛關注。最近研究指出使用帶有額外重金屬覆蓋層的重金屬 (HM) / 鐵磁體 (FM) 雙層結構，能決定性地切換 SOT-MRAM 的磁化量。本文利用微磁學模擬與漂移擴散自旋傳輸模型相結合，研究了利用此結構的 SOT-MRAM 的位元切換行為，指出該翻轉機制歸因於來自 HM 底部界面的自旋累積的不可忽略之負  $z$  分量，該自旋累積源於 HM 覆蓋層邊緣的自旋累積。此外，研究最後也指出器件參數對決定性切換和低功耗的重要性。本研究提供了關於使用額外 HM 覆蓋層的 SOT-MRAM 之決定性位元切換的基本原理討論，證明該結構未來有十足地潛力被推廣至實際應用中。

**關鍵字：** SOT-MRAM、決定性位元切換、微磁學模擬、漂移擴散自旋傳輸模型



# Abstract

Spin-orbit torque magnetic random-access memory (SOT-MRAM) has received extensive interest in the memory industry. Recent efforts have focused on a heavy metal (HM)/ferromagnet (FM) bilayer with an additional HM capping strip to deterministically switch the magnetization. This paper investigates the switching behaviors of SOT-MRAM utilizing this structure with micromagnetic simulations coupled to the drift-diffusion spin transport model. The mechanism is attributed to the non-negligible negative z-component from spin accumulation on the bottom HM interface, which originates from the associated accumulation at the edges of the HM capping strip. Moreover, device parameters are shown as crucial for deterministic switching and lower power consumption. This study provides fundamental insights into deterministic switching for SOT-MRAM with an additional HM capping strip, which can be readily adopted into practical applications.

**Keywords:** SOT-MRAM, deterministic switching, micromagnetic simulation, drift-diffusion spin transport model



# Table of Contents

	<b>Page</b>
<b>Approval Letter from the Oral Examination Committee</b>	<b>i</b>
<b>Acknowledgements</b>	<b>ii</b>
<b>摘要</b>	<b>iii</b>
<b>Abstract</b>	<b>iv</b>
<b>Table of Contents</b>	<b>v</b>
<b>List of Figures</b>	<b>vii</b>
<b>List of Tables</b>	<b>ix</b>
<b>Chapter 1 Introduction</b>	<b>1</b>
1.1 Current development of SOT-MRAM . . . . .	1
1.2 Deterministic switching of SOT-MRAM based on p-MTJs . . . . .	2
<b>Chapter 2 Research Methodology</b>	<b>5</b>
2.1 Micromagnetic simulations coupled to the drift-diffusion spin transport model . . . . .	5
2.2 Simulation of our focused system . . . . .	7
<b>Chapter 3 Results</b>	<b>9</b>
3.1 Deterministic switching of our device . . . . .	9
3.2 Investigation of the mechanism behind the deterministic switching . .	10

3.3	Current dependence of the switching behavior . . . . .	11
3.4	Device parameters dependence on the deterministic switching . . . . .	14
<b>Chapter 4</b>	<b>Results</b>	<b>16</b>
4.1	Deterministic switching of our device . . . . .	16
4.2	Investigation of the mechanism behind the deterministic switching . .	17
4.3	Current dependence of the switching behavior . . . . .	18
4.4	Device parameters dependence on the deterministic switching . . . .	21
<b>Chapter 5</b>	<b>Conclusion</b>	<b>23</b>
<b>References</b>		<b>24</b>

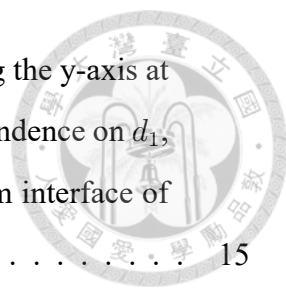




# List of Figures

1.1	(a) Schematic illustration of the SOT-MRAM structure utilizing the HM capping strip method,[1] (b) schematic diagram of the simulated SOT cell from this study, and (c) side view of the simulated SOT cell from this study.	4
3.1	Magnetization switching of the FL with $w = 25$ nm under a write pulse of $J = 8 \times 10^{12}$ A/m <sup>2</sup> for 2 ns. The deterministic switching is realized through the HM capping strip method. . . . .	10
3.2	(a) Temporal evolution of the magnetization for a conventional HM/FM ( $w = 50$ nm) during the current pulse. (b) The spin accumulation on the bottom HM interface along the y-axis. (c) The temporal evolution of the magnetization for an HM/FM with an additional HM capping strip ( $w = 25$ nm) during the current pulse. (d) The spin accumulation on the bottom HM interface along the y-axis. . . . .	12
3.3	(a) The spin accumulation in the HM, when $J$ is injected along the negative x-direction. (b) The spin accumulation on the bottom interface along the y-axis in (a). (c) The spin accumulation in the HM when $J$ is injected along the positive x-direction. (d) The spin accumulation on the bottom interface along the y-axis in (c). . . . .	12
3.4	(a) The complete magnetization switching under different $J$ , (b) the magnetization switching in one nanosecond under different $J$ , (c) spin accumulation distribution on the bottom HM interface under different $J$ , and (d) $m_r$ dependence on $J$ . . . . .	14





3.5 (a)  $J_c$  and  $m_{rc}$  dependence on  $w$ , (b)  $S_{y,z}$  distributions along the y-axis at the HM bottom interface of different  $w$ , (c)  $J_c$  and  $m_{rc}$  dependence on  $d_1$ , and (d)  $S_{y,z}$  distributions along the y-axis at the HM bottom interface of different  $d_1$ . . . . . 15

4.1 Magnetization switching of the FL with  $w = 25$  nm under a write pulse of  $J = 8 \times 10^{12}$  A/m<sup>2</sup> for 2 ns. The deterministic switching is realized through the HM capping strip method. . . . . 17

4.2 (a) Temporal evolution of the magnetization for a conventional HM/FM ( $w = 50$  nm) during the current pulse. (b) The spin accumulation on the bottom HM interface along the y-axis. (c) The temporal evolution of the magnetization for an HM/FM with an additional HM capping strip ( $w = 25$  nm) during the current pulse. (d) The spin accumulation on the bottom HM interface along the y-axis. . . . . 19

4.3 (a) The spin accumulation in the HM, when  $J$  is injected along the negative x-direction. (b) The spin accumulation on the bottom interface along the y-axis in (a). (c) The spin accumulation in the HM when  $J$  is injected along the positive x-direction. (d) The spin accumulation on the bottom interface along the y-axis in (c). . . . . 19

4.4 (a) The complete magnetization switching under different  $J$ , (b) the magnetization switching in one nanosecond under different  $J$ , (c) spin accumulation distribution on the bottom HM interface under different  $J$ , and (d)  $m_r$  dependence on  $J$ . . . . . 21

4.5 (a)  $J_c$  and  $m_{rc}$  dependence on  $w$ , (b)  $S_{y,z}$  distributions along the y-axis at the HM bottom interface of different  $w$ , (c)  $J_c$  and  $m_{rc}$  dependence on  $d_1$ , and (d)  $S_{y,z}$  distributions along the y-axis at the HM bottom interface of different  $d_1$ . . . . . 22



# List of Tables

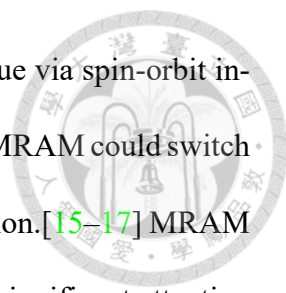
2.1	Input parameters used in the simulations. . . . .	7
-----	---------------------------------------------------	---



# Chapter 1 Introduction

## 1.1 Current development of SOT-MRAM

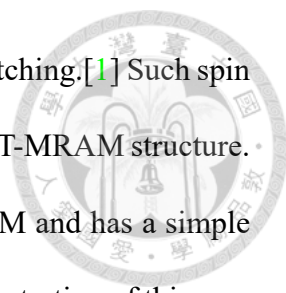
Rapid progress in the field of artificial intelligence and in-memory computing has heightened the demand for low power consumption and highly efficient devices.[2, 3] Magnetic random access memory (MRAM) has become a promising candidate among emerging memory technologies due to its non-volatility, low power consumption, fast read/write operations, and high endurance over other competing memory devices.[4, 5] MRAM is based on the magnetic tunnel junction (MTJ), which consists of two ferromagnetic layers and a thin insulator in the middle. The parallel and anti-parallel arrangements of the magnetization in ferromagnetic layers correspond to the low- and high-resistance states. Over the past decade, spin transfer torque magnetic random-access memory (STT-MRAM) has been among the most promising emerging memory technologies.[6] However, the writing speed, power consumption, and endurance of STT-MRAM still need further improvements. Researchers have recently demonstrated that spin-orbit torque (SOT) can induce magnetization switching in heavy-metal (HM)/ferromagnet (FM) bilayer systems, which may mitigate these issues in STT-MRAM.[7–11] In the SOT-driven magnetization switching, the current flows through the SOT channel and generates spin accumulation from the spin Hall effect (SHE)[12, 13] or the interfacial Rashba spin-orbit



coupling.[14] Spin accumulation under the ferromagnet exerts a torque via spin-orbit interactions to flip the magnetization. Compared to STT-MRAM, SOT-MRAM could switch the free layer (FL) magnetization faster with a lower power consumption.[15–17] MRAM with perpendicular magnetic tunnel junctions (p-MTJs) has received significant attention due to its high thermal stability and higher storage density these years.[18–20] However, SOT-MRAM based on p-MTJs cannot switch the magnetization deterministically because the current flow in the x-direction induces polarized spin along the y-direction in the HM layer. Accordingly, its stochastic nature is a major hindrance to its utilization in practical devices. To realize deterministic switching of a p-MTJ, an external magnetic field along the current direction is typically required to break the symmetry.[21, 22] However, the applied external magnetic field inevitably increases the difficulty of device manufacturing. Therefore, searching for a practical solution to deterministic switching in SOT-MRAM based on p-MTJ is vital for modern spintronics technologies.[23, 24] Several promising approaches have been developed, such as interface exchange coupling,[25, 26] tilted magnetic anisotropy,[27, 28] using a combination of STT and SOT,[29–32] lateral structural asymmetry,[1, 33–37] or gradient spin current.[1, 38–40]

## **1.2 Deterministic switching of SOT-MRAM based on p-MTJs**

The deterministic switching utilizing lateral structural asymmetry relies on an additional out-of-plane effective magnetic field.[24, 33] It could be realized by using a wedge-shaped ferromagnet,[37] insertion of an asymmetric layer,[34–36] or utilizing an asymmetric Ta layer after oxidation.[33] Recent experiments have revealed that SOT devices



with additional HM capping strips could also enable deterministic switching.[1] Such spin logic devices have the potential to create a field-free perpendicular SOT-MRAM structure. The design keeps the homogeneity of the magnetic property in the FM and has a simple structure without incorporating any additional layers. A schematic illustration of this proposed SOT-MRAM structure is shown in Fig. 1(a). However, the microscopic creation of the additional out-of-plane effective magnetic field and quantitative understanding of the switching behaviors need clarification for practical memory device applications. This study helps understand how an HM capping strip achieves deterministic switching in SOT-MRAM through micromagnetic simulations coupled to a self-consistent drift-diffusion spin transport solver. The three-dimensional spin transport solver self-consistently calculates the charge currents, spin currents, and spin accumulations for arbitrary geometries and multi-layer structures without importing a computed current density.[41–43] The strength of spin torques can be calculated from the given spin transport parameters.[41–43] The model has also been shown to be superior to incorporating analytical representations of different spin torques in the Landau–Lifshitz–Gilbert (LLG) equation for non-uniform charge and spin currents, and when various spin torques are present.[41–43] Therefore, self-consistent spin torque is a more accurate approach to handle the non-uniform spin current and asymmetric geometry in the HM capping strip method. We show that the spin accumulation from the edges of the HM capping strip causes various distributions of spin accumulation on the bottom HM interface, which leads to deterministic switching. Moreover, the switching characteristics for different device parameters was also investigated.

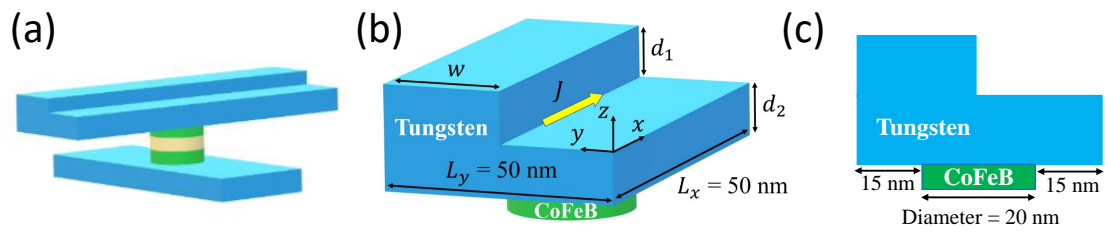


Figure 1.1: (a) Schematic illustration of the SOT-MRAM structure utilizing the HM capping strip method,[1] (b) schematic diagram of the simulated SOT cell from this study, and (c) side view of the simulated SOT cell from this study.



## Chapter 2 Research Methodology

### 2.1 Micromagnetic simulations coupled to the drift-diffusion spin transport model

To understand magnetic dynamics with gradient spin current, we perform micromagnetic simulations using Boris Computational Spintronics,[44] which is a high-performance magnetic and spin transport modeling software. In the simulations, the magnetization switching dynamics are modeled using the LLG equation containing the total spin torque:

$$\frac{\partial \mathbf{m}}{\partial t} = -\gamma \mathbf{m} \times \mathbf{H}_{eff} + \alpha \mathbf{m} \times \frac{\partial \mathbf{m}}{\partial t} + \frac{\mathbf{T}_s}{M_s}, \quad (2.1)$$

where  $\gamma = \mu_0 |\gamma_e|$ ,  $\gamma_e = -g\mu_B/\hbar$  is the electron gyromagnetic ratio,  $\mathbf{m}$  is the unit vector along the magnetization of FL,  $M_s$  is the saturation magnetization,  $\alpha$  is the damping constant,  $\mathbf{T}_s$  is the total spin torque, and the effective field  $\mathbf{H}_{eff}$  contains all the magnetic field contributions, including the Oersted field, demagnetization field, uniaxial magnetocrystalline anisotropy, and exchange interaction. The total spin torque includes contributions from the STT, SOT, and interfacial spin-transfer torque (ISTT), which can be computed self-consistently using the drift-diffusion model.[42, 45–47] Within the drift-diffusion spin transport solver, the spin accumulation is solved each time step to self-consistently com-

pute the spin torque. The equation of motion for spin accumulation is modeled by:

$$\frac{\partial \mathbf{S}}{\partial t} = -\nabla \cdot \mathbf{J}_S - D_e \left( \frac{\mathbf{S}}{\lambda_{sf}^2} + \frac{\mathbf{S} \times \mathbf{m}}{\lambda_J^2} + \frac{\mathbf{m} \times (\mathbf{S} \times \mathbf{m})}{\lambda_\phi^2} \right), \quad (2.2)$$

where  $\mathbf{S}$  is the spin accumulation,  $\mathbf{J}_S$  is the spin polarization current density,  $D_e$  is the electron diffusion constant,  $\lambda_{sf}$  is the spin-flip length,  $\lambda_J$  is the exchange rotation length, and  $\lambda_\phi$  is the spin dephasing length. Interfacial spin torques may be computed as:

$$\mathbf{T}_s^i = \frac{g\mu_B}{ed_F} [Re \{G^{\uparrow\downarrow}\} \mathbf{m} \times (\mathbf{m} \times \Delta \mathbf{V}_s) + Im \{G^{\uparrow\downarrow}\} \mathbf{m} \times \Delta \mathbf{V}_s], \quad (2.3)$$

where  $G^{\uparrow\downarrow}$  is the spin-mixing conductance,  $d_F$  is the ferromagnetic layer thickness, and  $\mathbf{V}_s$  is the spin chemical potential drop across the HM/FM interface, where  $\mathbf{V}_s = (D_e/\sigma)(e/\mu_B)\mathbf{S}$  and  $\sigma$  is the electrical conductivity. Bulk spin torques are obtained from the spin accumulation as:

$$\mathbf{T}_s^b = -\frac{D_e}{\lambda_J^2} \mathbf{m} \times \mathbf{S} - \frac{D_e}{\lambda_\phi^2} \mathbf{m} \times (\mathbf{m} \times \mathbf{S}). \quad (2.4)$$

This work uses a simple W/CoFeB/MgO structure to realize deterministic switching based on the HM capping strip method, which can be readily adopted in magnetic tunnel junctions.[48–50] The parameters utilized in the simulations are listed in Table 1. The LLG equation is computed with a mesh size of 1 nm x 1 nm x 1 nm. For spin transport calculations, the spin accumulation is computed with a mesh size of 1 nm x 1 nm x 0.1 nm. The discussion presented herein focuses on the properties of MTJs with a diameter of 20 nm and thickness of 1 nm as these are the dimensions most likely used in real applications.





Parameters	Numerical values	Description
$A$	$2 \times 10^{-11}$ J/m	Exchange constant
$M_s$	$1 \times 10^6$ A/m	Saturation magnetization
$K$	$8.50 \times 10^5$ J/m <sup>3</sup>	Magnetic anisotropy [19, 28, 31, 51]
$temp$	0 K	Absolute temperature
$\alpha$	0.02	Damping constant
$\sigma_{CoFeB}$	$3.03 \times 10^5$ S/m	Conductivity of CoFeB [48]
$\sigma_W$	$2.70 \times 10^5$ S/m	Conductivity of tungsten [48]
$D_{CoFeB}$	0.001 m/s <sup>2</sup>	Diffusion constant of CoFeB [48]
$D_W$	0.0002 m/s <sup>2</sup>	Diffusion constant of tungsten [52]
$\lambda_{sf,W}$	2.5 nm	Spin-flip length of tungsten [48]
$\lambda_{sf,CoFeB}$	10 nm	Spin-flip length of CoFeB
$\lambda_{J,CoFeB}$	2 nm	Exchange rotation length of CoFeB
$\lambda_{\phi,CoFeB}$	4 nm	Spin dephasing length of CoFeB
$P$	0.52	Spin polarization of CoFeB[53]
$\theta_{SH}$	0.3	Spin Hall angle of tungsten [54]
$G^{\uparrow\downarrow}$	$0.39 + i0.13$ PS/m <sup>2</sup>	Spin mixing conductance[48]

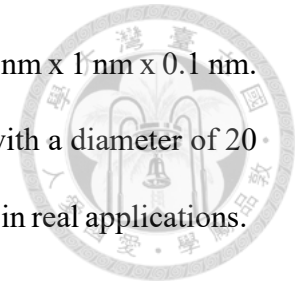
Table 2.1: Input parameters used in the simulations.

## 2.2 Simulation of our focused system

This work uses a simple W/CoFeB/MgO structure to realize deterministic switching based on the HM capping strip method, which can be readily adopted in magnetic tunnel junctions.[48–50] The parameters utilized in the simulations are listed in Table 1. The LLG equation is computed with a mesh size of 1 nm x 1 nm x 1 nm. For spin transport

calculations, the spin accumulation is computed with a mesh size of 1 nm x 1 nm x 0.1 nm.

The discussion presented herein focuses on the properties of MTJs with a diameter of 20 nm and thickness of 1 nm as these are the dimensions most likely used in real applications.





## Chapter 3 Results

### 3.1 Deterministic switching of our device

Figures 1(b) and 1(c) show the simulated structure. The HM capping strip has a variable width of  $w$  and a thickness of  $d_1$  nm. The bottom HM layer under has a width of 50 nm and a thickness of  $d_2$  nm. Both HM layers have lengths of 50 nm along the x-direction. Figure 2 illustrates the simulated temporal evolutions of the average magnetization components ( $M_{x,y,z}/M_s$ ) for  $w = 25$  nm,  $d_1 = 2$  nm, and  $d_2 = 3$  nm. In the simulations, the FL magnetization starts from an initial state of  $M_z/M_s = +1$ . The pulse current density  $J$  is injected into the HM along the negative x-direction with a duration of 2 ns, which is imposed from  $t = 0$  to 2 ns. After 2 ns,  $J$  is turned off, and the magnetization switches to the negative z-axis through the relaxation process. In a conventional HM/FM, there is no additional HM capping strip. The  $M_z/M_s$  approaches 0 and  $M_y/M_s$  approaches +1 after the current pulse, which leads to a non-deterministic state when the current is removed. However,  $M_z/M_s$  crosses over 0 and reaches a negative remnant value  $m_r$ . We define the remnant value  $m_r$  as the  $M_z/M_s$  when the magnetization reaches a steady state during the current pulse duration. After removing the current,  $M_z/M_s$  proceeds toward  $M_z/M_s = -1$  and causes deterministic switching.

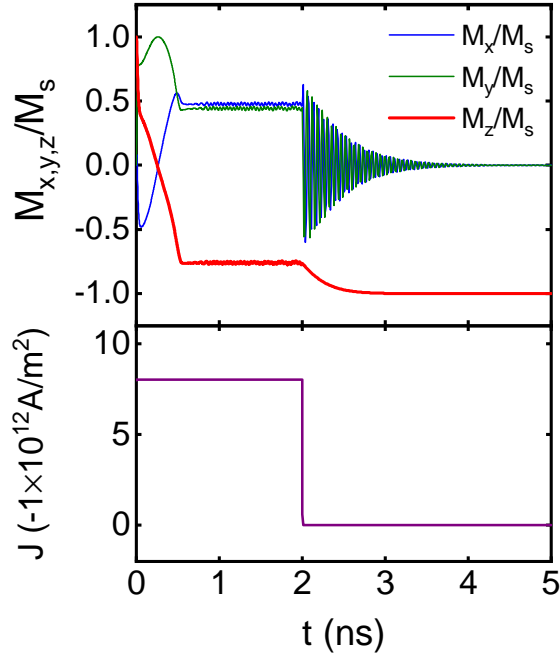
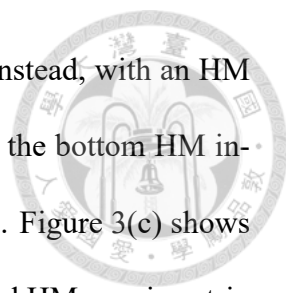


Figure 3.1: Magnetization switching of the FL with  $w = 25$  nm under a write pulse of  $J = 8 \times 10^{12}$  A/m<sup>2</sup> for 2 ns. The deterministic switching is realized through the HM capping strip method.

## 3.2 Investigation of the mechanism behind the deterministic switching

We also investigate the mechanism behind the HM-capping-strip-induced deterministic switching. The spin accumulation distribution on the bottom HM interface is at the heart of understanding deterministic switching. Figure 3(a) shows the magnetization temporal evolution of a conventional HM/FM ( $w = 50$  nm) during the same considered duration. Figure 3(b) shows the spin accumulation components ( $S_{x,y,z}$ ) along the y-axis on the bottom HM interface at  $x = 25$  nm at  $t = 0$ , where the cartesian coordinate system is defined in Fig. 1(a). The polarized spin accumulation above the FL is directed along the positive y-direction and contributes to a large spin torque that drags the magnetization toward the positive y-axis. The same simulation with a larger current pushes the magnetization to an equilibrium state with  $M_z/M_s$  closer to zero and  $M_y/M_s$  closer to 1.



However, the magnetization does not switch to a negative  $M_z/M_s$ . Instead, with an HM strip capping on the HM layer, the spin accumulation distribution on the bottom HM interface varies, leading to different magnetization switching behaviors. Figure 3(c) shows the magnetization temporal evolution of the HM/FM with an additional HM capping strip ( $w = 25$  nm) during the considered current duration. Figure 3(d) shows  $S_{x,y,z}$  along the y-axis on the bottom HM interface at  $x = 25$  nm at  $t = 0$ . In contrast to the conventional HM/FM, some non-negligible negative  $S_z$  is observed near the center y position, which is immediately above the FL. This negative  $S_z$  induces an additional negative z-direction spin torque when  $M_x/M_s = 0$ ,  $M_y/M_s = +1$ , and  $M_z/M_s = 0$  is reached. Therefore, a negative  $m_r$  is observed under sufficiently large  $J$ . This is the critical factor of deterministic switching for the proposed structure. To understand the origin of this non-negligible  $S_z$  on the bottom HM interface, Figs. 4(a) and 4(b) show the origination from the negative z-direction spin on the edge of the HM capping strip. By characterizing the system with an accurate spin-flip length  $\lambda_{sf}$  of tungsten, the drift-diffusion spin transport solver with a negative z spin on the edge of the HM capping strip leads to a non-negligible negative  $S_z$  on the bottom HM interface. Further, Figs. 4(c) and 4(d) show that the spin accumulation along the y-axis on the bottom HM interface has an opposing polarity when applying the opposite direction of  $J$ . Thus, the magnetization switches from  $M_z/M_s = -1$  to  $M_z/M_s = 1$  by changing the polarity of the current.

### 3.3 Current dependence of the switching behavior

Additional detailed information can be obtained from the time evolution of  $M_z/M_s$  under various  $J$ . As seen in Fig. 5(a) and 5(b),  $M_z/M_s$  reaches different  $m_r$  under various  $J$ . For  $J$  less than  $7 \times 10^{12} \text{ Am}^{-2}$ ,  $m_r$  is positive, and  $M_z/M_s$  returns to the positive z-axis

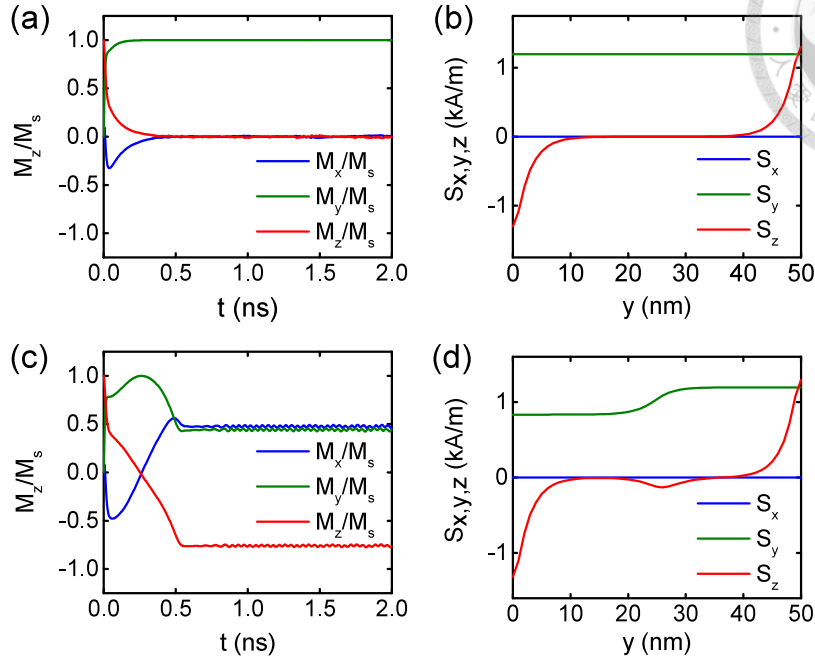
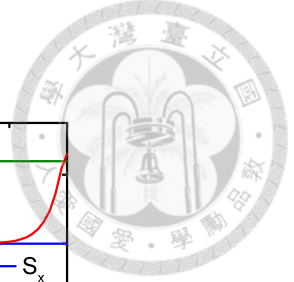


Figure 3.2: (a) Temporal evolution of the magnetization for a conventional HM/FM ( $w = 50$  nm) during the current pulse. (b) The spin accumulation on the bottom HM interface along the  $y$ -axis. (c) The temporal evolution of the magnetization for an HM/FM with an additional HM capping strip ( $w = 25$  nm) during the current pulse. (d) The spin accumulation on the bottom HM interface along the  $y$ -axis.

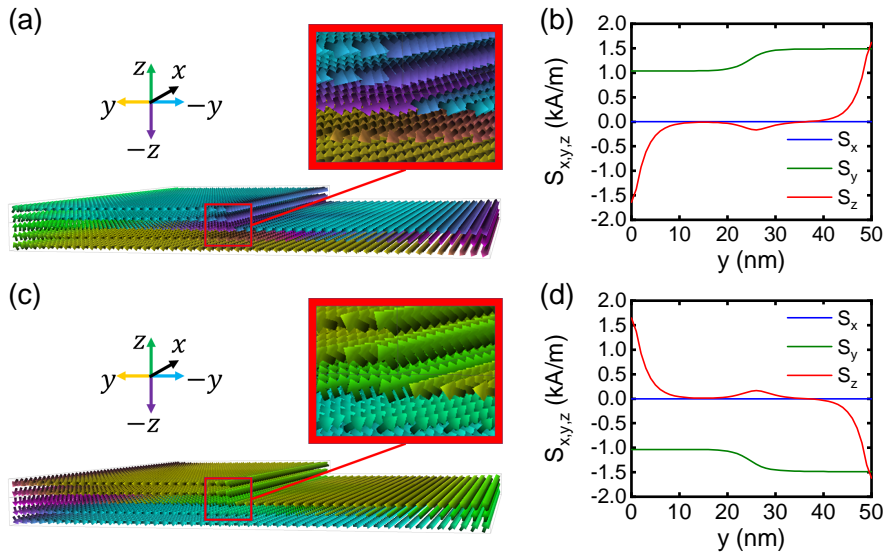
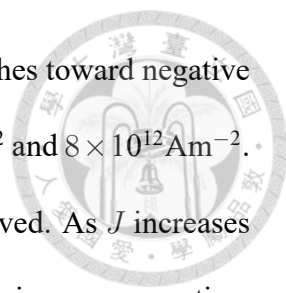


Figure 3.3: (a) The spin accumulation in the HM, when  $J$  is injected along the negative  $x$ -direction. (b) The spin accumulation on the bottom interface along the  $y$ -axis in (a). (c) The spin accumulation in the HM when  $J$  is injected along the positive  $x$ -direction. (d) The spin accumulation on the bottom interface along the  $y$ -axis in (c).



after the current pulse ends. As the magnitude of  $J$  increases,  $m_r$  pushes toward negative values, where the critical current density ( $J_c$ ) is between  $6 \times 10^{12} \text{Am}^{-2}$  and  $8 \times 10^{12} \text{Am}^{-2}$ . Once  $J$  reaches  $8 \times 10^{12} \text{Am}^{-2}$ , a large negative value for  $m_r$  is observed. As  $J$  increases more,  $m_r$  pushes back toward smaller negative values instead of becoming more negative. Figure 5(c) shows the  $S_y$  and  $S_z$  distribution along the y-axis with an increasing  $J$ . When  $J$  is smaller than  $J_c$ , the spin torque originates from the spin accumulation and competes with the anisotropy field, which gives different  $m_r$  values. As  $J$  reaches  $J_c$ , abrupt variations of  $m_r$  occur because the negative z-direction torque that originates from the negative  $S_z$  drags  $M_z/M_s$  toward negative values when  $M_y/M_s = +1$  is reached. Once  $M_z/M_s < 0$ , the negative z-direction anisotropy field has a strong effect on the magnetization. Thus,  $M_z/M_s$  reaches a large negative  $m_r$  with almost the same absolute value. As  $J$  increases further,  $m_r$  pushes back toward smaller negative values due to the strong effect of  $S_y$  at the HM/FM interface, just as what it used to be in the conventional HM/FM bilayer without an HM capping strip.

Figure 5(d) summarizes  $m_r$  under different currents during the pulse duration. The  $m_r$  depends strongly on the current direction and magnitude, which indicates that deterministic bipolar switching can be achieved by changing the polarity of the current. After the current pulse stops,  $M_z/M_s$  eventually relaxes toward the positive or negative z-directions. A larger  $m_r$  results in improved switching behaviors because  $m_r$  prevents the magnetization from stochastically switching under the interference of thermal fluctuations. Furthermore, Fig. 5(a) indicates that a larger  $m_r$  induces a faster relaxation process when the current is removed, which gives a faster operating speed for the MRAM cell. Therefore, a larger current does not guarantee a higher switching speed. Instead,  $J$  with a magnitude slightly larger than  $J_c$  gives the ideal results.

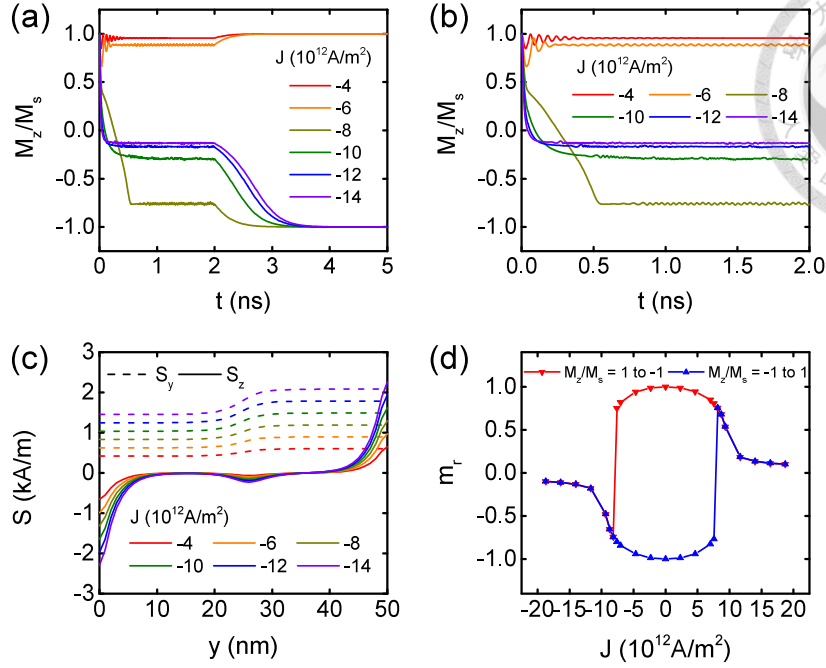


Figure 3.4: (a) The complete magnetization switching under different  $J$ , (b) the magnetization switching in one nanosecond under different  $J$ , (c) spin accumulation distribution on the bottom HM interface under different  $J$ , and (d)  $m_r$  dependence on  $J$ .

### 3.4 Device parameters dependence on the deterministic switching

We define  $m_r$  at  $J = J_c$  as the critical  $m_r$  ( $m_{rc}$ ). The Figure 6(a) summarizes the  $J_c$  and  $m_{rc}$  dependence on  $w$  when switching from  $M_z/M_s = +1$  to  $M_z/M_s = -1$  and vice versa. The absolute values of  $m_{rc}$  are relatively large from  $w = 20$  nm to  $w = 35$  nm but quickly reduce when  $w < 20$  nm or  $w > 35$  nm. The relationships are explained by the  $S_{y,z}$  distribution along the  $y$ -axis at the HM bottom interface under constant current in Fig. 6(b). The FL lies between  $y = 15$  nm and  $y = 35$  nm. Upon the negative  $z$ -direction spin being out of range, the absolute values of  $m_r$  decrease quickly toward zero, and the deterministic switching no longer sustains. The  $J_c$  dependence on  $w$  is explained by the  $S_y$  value, which is the main source of the in-plane field. Larger  $w$  results in a higher average value of  $S_y$  under the same  $J$ . Therefore, the  $J_c$  reduces with a larger  $w$ . In conclusion,  $w$



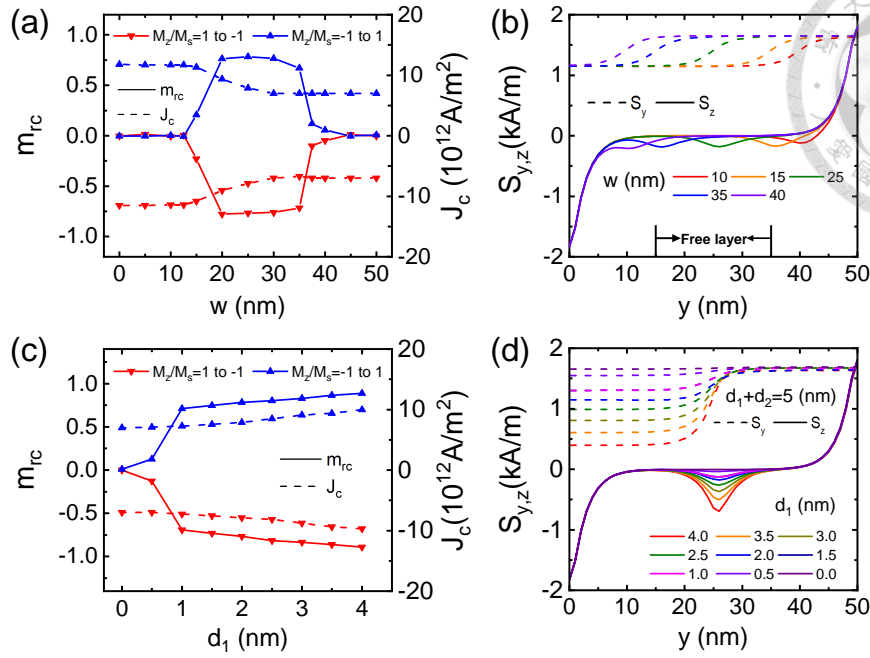


Figure 3.5: (a)  $J_c$  and  $m_{rc}$  dependence on  $w$ , (b)  $S_{y,z}$  distributions along the  $y$ -axis at the HM bottom interface of different  $w$ , (c)  $J_c$  and  $m_{rc}$  dependence on  $d_1$ , and (d)  $S_{y,z}$  distributions along the  $y$ -axis at the HM bottom interface of different  $d_1$ .

can be designed larger to lower  $J_c$  but should not be designed too large to keep the absolute value of  $m_{rc}$  large enough for deterministic switching. The Figure 6(c) summarizes the  $J_c$  and  $m_{rc}$  dependence on  $d_1$  under the condition  $d_1 + d_2 = 5$  nm when switching from  $M_z/M_s = +1$  to  $M_z/M_s = -1$  and vice versa. The absolute value of  $m_{rc}$  positively correlates with  $d_1$ . However, it quickly reduces to zero when  $d_1$  approaches zero due to the vanishing of the negative  $z$ -direction spin. The relationships are explained by the  $S_{y,z}$  distribution along the  $y$ -axis at the HM bottom interface under constant current in Fig. 6(d). Similarly, the  $J_c$  dependence on  $d_1$  can be understood from the relative strength of the average  $S_y$  value. With a larger  $d_1$ , the negative  $S_z$  on the HM bottom interface amplifies significantly. The combination effect of  $S_y$  and  $S_z$  then leads to the result in Fig. 6(c).



## Chapter 4 Results

### 4.1 Deterministic switching of our device

Figures 1(b) and 1(c) show the simulated structure. The HM capping strip has a variable width of  $w$  and a thickness of  $d_1$  nm. The bottom HM layer under has a width of 50 nm and a thickness of  $d_2$  nm. Both HM layers have lengths of 50 nm along the x-direction. Figure 2 illustrates the simulated temporal evolutions of the average magnetization components ( $M_{x,y,z}/M_s$ ) for  $w = 25$  nm,  $d_1 = 2$  nm, and  $d_2 = 3$  nm. In the simulations, the FL magnetization starts from an initial state of  $M_z/M_s = +1$ . The pulse current density  $J$  is injected into the HM along the negative x-direction with a duration of 2 ns, which is imposed from  $t = 0$  to 2 ns. After 2 ns,  $J$  is turned off, and the magnetization switches to the negative z-axis through the relaxation process. In a conventional HM/FM, there is no additional HM capping strip. The  $M_z/M_s$  approaches 0 and  $M_y/M_s$  approaches +1 after the current pulse, which leads to a non-deterministic state when the current is removed. However,  $M_z/M_s$  crosses over 0 and reaches a negative remnant value  $m_r$ . We define the remnant value  $m_r$  as the  $M_z/M_s$  when the magnetization reaches a steady state during the current pulse duration. After removing the current,  $M_z/M_s$  proceeds toward  $M_z/M_s = -1$  and causes deterministic switching.

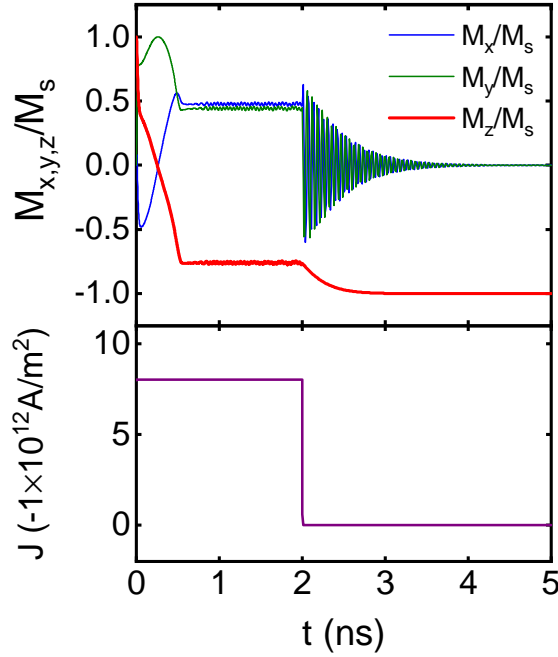
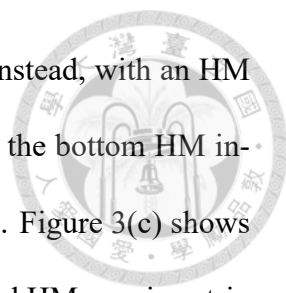


Figure 4.1: Magnetization switching of the FL with  $w = 25$  nm under a write pulse of  $J = 8 \times 10^{12}$  A/m<sup>2</sup> for 2 ns. The deterministic switching is realized through the HM capping strip method.

## 4.2 Investigation of the mechanism behind the deterministic switching

We also investigate the mechanism behind the HM-capping-strip-induced deterministic switching. The spin accumulation distribution on the bottom HM interface is at the heart of understanding deterministic switching. Figure 3(a) shows the magnetization temporal evolution of a conventional HM/FM ( $w = 50$  nm) during the same considered duration. Figure 3(b) shows the spin accumulation components ( $S_{x,y,z}$ ) along the y-axis on the bottom HM interface at  $x = 25$  nm at  $t = 0$ , where the cartesian coordinate system is defined in Fig. 1(a). The polarized spin accumulation above the FL is directed along the positive y-direction and contributes to a large spin torque that drags the magnetization toward the positive y-axis. The same simulation with a larger current pushes the magnetization to an equilibrium state with  $M_z/M_s$  closer to zero and  $M_y/M_s$  closer to 1.



However, the magnetization does not switch to a negative  $M_z/M_s$ . Instead, with an HM strip capping on the HM layer, the spin accumulation distribution on the bottom HM interface varies, leading to different magnetization switching behaviors. Figure 3(c) shows the magnetization temporal evolution of the HM/FM with an additional HM capping strip ( $w = 25$  nm) during the considered current duration. Figure 3(d) shows  $S_{x,y,z}$  along the y-axis on the bottom HM interface at  $x = 25$  nm at  $t = 0$ . In contrast to the conventional HM/FM, some non-negligible negative  $S_z$  is observed near the center y position, which is immediately above the FL. This negative  $S_z$  induces an additional negative z-direction spin torque when  $M_x/M_s = 0$ ,  $M_y/M_s = +1$ , and  $M_z/M_s = 0$  is reached. Therefore, a negative  $m_r$  is observed under sufficiently large  $J$ . This is the critical factor of deterministic switching for the proposed structure. To understand the origin of this non-negligible  $S_z$  on the bottom HM interface, Figs. 4(a) and 4(b) show the origination from the negative z-direction spin on the edge of the HM capping strip. By characterizing the system with an accurate spin-flip length  $\lambda_{sf}$  of tungsten, the drift-diffusion spin transport solver with a negative z spin on the edge of the HM capping strip leads to a non-negligible negative  $S_z$  on the bottom HM interface. Further, Figs. 4(c) and 4(d) show that the spin accumulation along the y-axis on the bottom HM interface has an opposing polarity when applying the opposite direction of  $J$ . Thus, the magnetization switches from  $M_z/M_s = -1$  to  $M_z/M_s = 1$  by changing the polarity of the current.

### 4.3 Current dependence of the switching behavior

Additional detailed information can be obtained from the time evolution of  $M_z/M_s$  under various  $J$ . As seen in Fig. 5(a) and 5(b),  $M_z/M_s$  reaches different  $m_r$  under various  $J$ . For  $J$  less than  $7 \times 10^{12} \text{ Am}^{-2}$ ,  $m_r$  is positive, and  $M_z/M_s$  returns to the positive z-axis

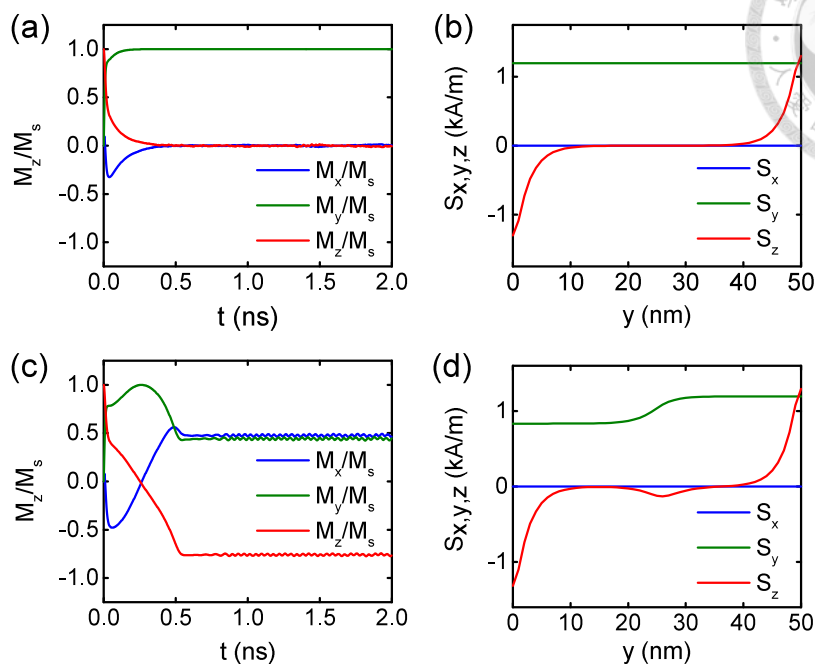
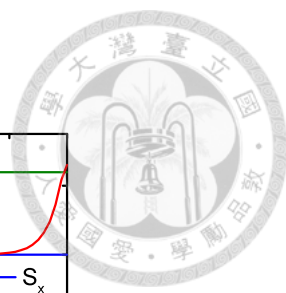


Figure 4.2: (a) Temporal evolution of the magnetization for a conventional HM/FM ( $w = 50$  nm) during the current pulse. (b) The spin accumulation on the bottom HM interface along the  $y$ -axis. (c) The temporal evolution of the magnetization for an HM/FM with an additional HM capping strip ( $w = 25$  nm) during the current pulse. (d) The spin accumulation on the bottom HM interface along the  $y$ -axis.

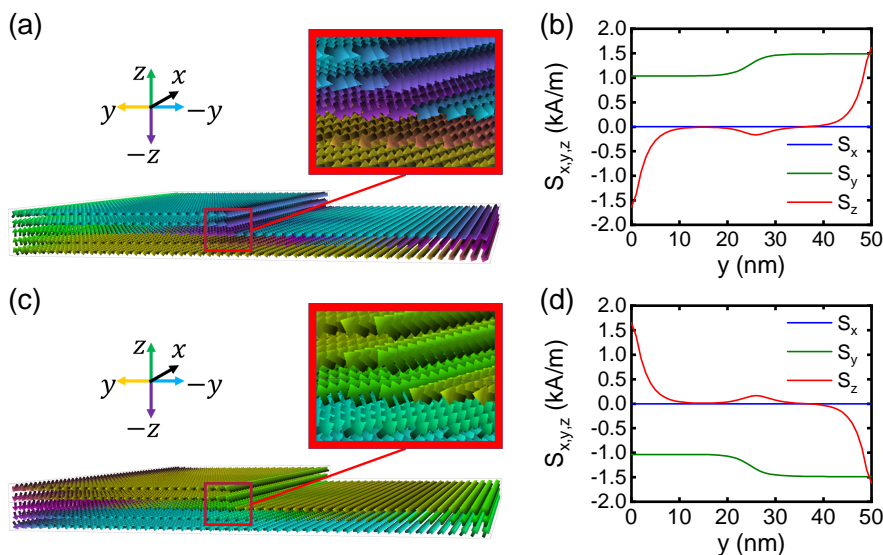
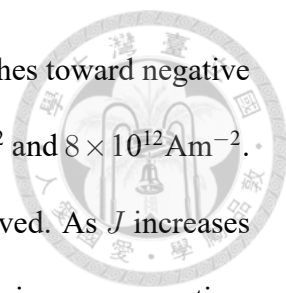


Figure 4.3: (a) The spin accumulation in the HM, when  $J$  is injected along the negative  $x$ -direction. (b) The spin accumulation on the bottom interface along the  $y$ -axis in (a). (c) The spin accumulation in the HM when  $J$  is injected along the positive  $x$ -direction. (d) The spin accumulation on the bottom interface along the  $y$ -axis in (c).



after the current pulse ends. As the magnitude of  $J$  increases,  $m_r$  pushes toward negative values, where the critical current density ( $J_c$ ) is between  $6 \times 10^{12} \text{Am}^{-2}$  and  $8 \times 10^{12} \text{Am}^{-2}$ . Once  $J$  reaches  $8 \times 10^{12} \text{Am}^{-2}$ , a large negative value for  $m_r$  is observed. As  $J$  increases more,  $m_r$  pushes back toward smaller negative values instead of becoming more negative. Figure 5(c) shows the  $S_y$  and  $S_z$  distribution along the y-axis with an increasing  $J$ . When  $J$  is smaller than  $J_c$ , the spin torque originates from the spin accumulation and competes with the anisotropy field, which gives different  $m_r$  values. As  $J$  reaches  $J_c$ , abrupt variations of  $m_r$  occur because the negative z-direction torque that originates from the negative  $S_z$  drags  $M_z/M_s$  toward negative values when  $M_y/M_s = +1$  is reached. Once  $M_z/M_s < 0$ , the negative z-direction anisotropy field has a strong effect on the magnetization. Thus,  $M_z/M_s$  reaches a large negative  $m_r$  with almost the same absolute value. As  $J$  increases further,  $m_r$  pushes back toward smaller negative values due to the strong effect of  $S_y$  at the HM/FM interface, just as what it used to be in the conventional HM/FM bilayer without an HM capping strip.

Figure 5(d) summarizes  $m_r$  under different currents during the pulse duration. The  $m_r$  depends strongly on the current direction and magnitude, which indicates that deterministic bipolar switching can be achieved by changing the polarity of the current. After the current pulse stops,  $M_z/M_s$  eventually relaxes toward the positive or negative z-directions. A larger  $m_r$  results in improved switching behaviors because  $m_r$  prevents the magnetization from stochastically switching under the interference of thermal fluctuations. Furthermore, Fig. 5(a) indicates that a larger  $m_r$  induces a faster relaxation process when the current is removed, which gives a faster operating speed for the MRAM cell. Therefore, a larger current does not guarantee a higher switching speed. Instead,  $J$  with a magnitude slightly larger than  $J_c$  gives the ideal results.

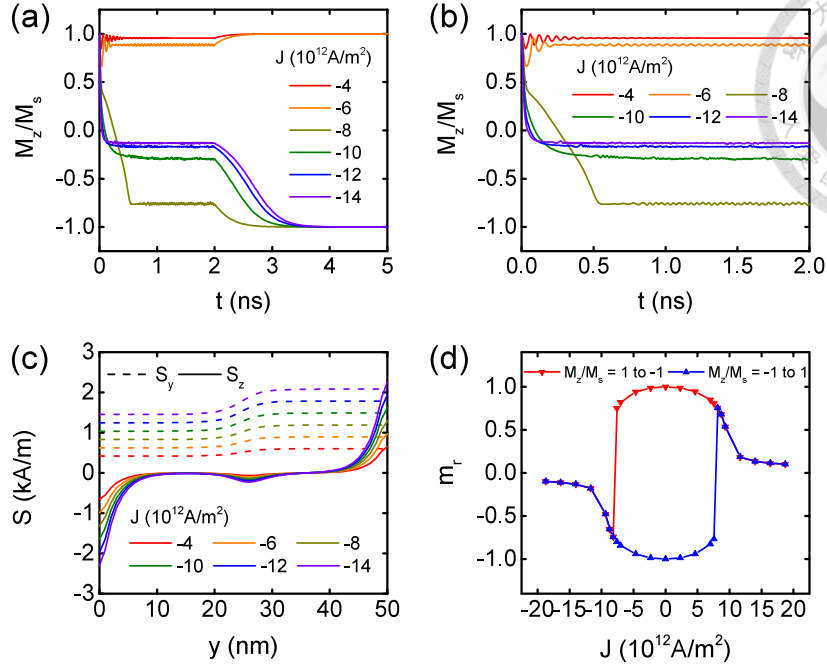


Figure 4.4: (a) The complete magnetization switching under different  $J$ , (b) the magnetization switching in one nanosecond under different  $J$ , (c) spin accumulation distribution on the bottom HM interface under different  $J$ , and (d)  $m_r$  dependence on  $J$ .

## 4.4 Device parameters dependence on the deterministic switching

We define  $m_r$  at  $J = J_c$  as the critical  $m_r$  ( $m_{rc}$ ). The Figure 6(a) summarizes the  $J_c$  and  $m_{rc}$  dependence on  $w$  when switching from  $M_z/M_s = +1$  to  $M_z/M_s = -1$  and vice versa. The absolute values of  $m_{rc}$  are relatively large from  $w = 20$  nm to  $w = 35$  nm but quickly reduce when  $w < 20$  nm or  $w > 35$  nm. The relationships are explained by the  $S_{y,z}$  distribution along the  $y$ -axis at the HM bottom interface under constant current in Fig. 6(b). The FL lies between  $y = 15$  nm and  $y = 35$  nm. Upon the negative  $z$ -direction spin being out of range, the absolute values of  $m_r$  decrease quickly toward zero, and the deterministic switching no longer sustains. The  $J_c$  dependence on  $w$  is explained by the  $S_y$  value, which is the main source of the in-plane field. Larger  $w$  results in a higher average value of  $S_y$  under the same  $J$ . Therefore, the  $J_c$  reduces with a larger  $w$ . In conclusion,  $w$

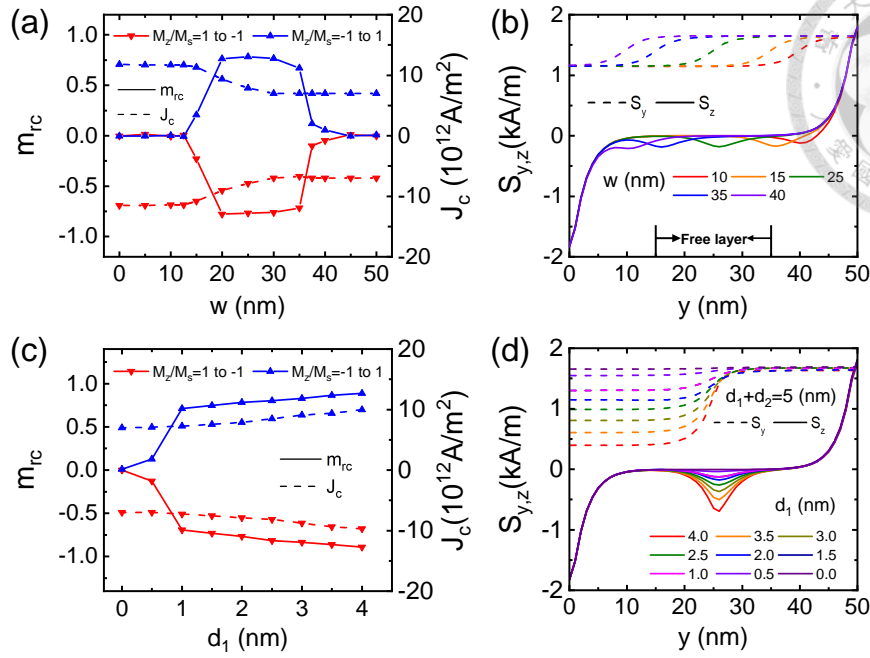


Figure 4.5: (a)  $J_c$  and  $m_{rc}$  dependence on  $w$ , (b)  $S_{y,z}$  distributions along the  $y$ -axis at the HM bottom interface of different  $w$ , (c)  $J_c$  and  $m_{rc}$  dependence on  $d_1$ , and (d)  $S_{y,z}$  distributions along the  $y$ -axis at the HM bottom interface of different  $d_1$ .

can be designed larger to lower  $J_c$  but should not be designed too large to keep the absolute value of  $m_{rc}$  large enough for deterministic switching. The Figure 6(c) summarizes the  $J_c$  and  $m_{rc}$  dependence on  $d_1$  under the condition  $d_1 + d_2 = 5$  nm when switching from  $M_z/M_s = +1$  to  $M_z/M_s = -1$  and vice versa. The absolute value of  $m_{rc}$  positively correlates with  $d_1$ . However, it quickly reduces to zero when  $d_1$  approaches zero due to the vanishing of the negative  $z$ -direction spin. The relationships are explained by the  $S_{y,z}$  distribution along the  $y$ -axis at the HM bottom interface under constant current in Fig. 6(d). Similarly, the  $J_c$  dependence on  $d_1$  can be understood from the relative strength of the average  $S_y$  value. With a larger  $d_1$ , the negative  $S_z$  on the HM bottom interface amplifies significantly. The combination effect of  $S_y$  and  $S_z$  then leads to the result in Fig. 6(c).






## Chapter 5 Conclusion


We investigate the switching behaviors for W/CoFeB/MgO through micromagnetic simulations coupled with a self-consistent spin transport solver. The underlying mechanism of the deterministic switching is clarified, which is well understood from the spin accumulation distribution on the bottom HM interface along the gradient direction. A non-negligible  $S_z$  on the bottom HM interface is crucial for bipolar switching, and the sign of  $m_r$  determines the final magnetization state. Moreover,  $m_{rc}$  and  $J_c$  dependence at various device parameters are obtained and well-understood. The SOT-MRAM based on an additional HM capping strip provides a new way to achieve magnetic memory operations. These findings could help guide the practical application of SOT-driven deterministic switching without external fields.



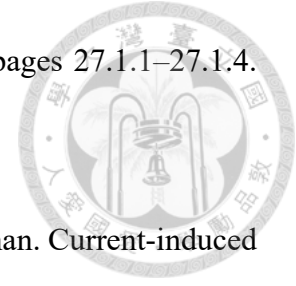
## References

- [1] Yucai Li, Nan Zhang, and Kaiyou Wang. Spin logic operations based on magnetization switching by asymmetric spin current. Sci. China Inf. Sci., 65(2):122404, 2022.
- [2] Chunmeng Dou, Wei Hao Chen, Yi Ju Chen, Huan Ting Lin, Wei Yu Lin, Mon Shu Ho, and Meng Fan Chang. Challenges of emerging memory and memristor based circuits: Nonvolatile logics, iot security, deep learning and neuromorphic computing. In 2017 IEEE 12th international conference on ASIC (ASICON), pages 140–143. IEEE, 2017.
- [3] Ranjana Godse, Adam McPadden, Vipin Patel, and Jung Yoon. Memory technology enabling the next artificial intelligence revolution. In 2018 IEEE Nanotechnology Symposium (ANTS), pages 1–4. IEEE, 2018.
- [4] S Yuasa, A Fukushima, K Yakushiji, T Nozaki, M Konoto, H Maehara, H Kubota, T Taniguchi, H Arai, H Imamura, et al. Future prospects of mram technologies. In 2013 IEEE International Electron Devices Meeting, pages 3.1.1–3.1.4. IEEE, 2013.
- [5] Chi Feng Pai and Denny D Tang. Magnetic Memory Technology: Spin-transfer-torque Mram and Beyond. John Wiley & Sons, 2020.

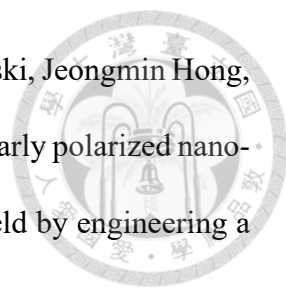
- 
- [6] Rachid Sbiaa and SN Piramanayagam. Recent developments in spin transfer torque mram. Phys. Status Solidi RRL, 11(12):1700163, 2017.
- [7] A. Manchon and S. Zhang. Theory of spin torque due to spin-orbit coupling. Phys. Rev. B, 79:094422, Mar 2009.
- [8] Alexandr Chernyshov, Mason Overby, Xinyu Liu, Jacek K Furdyna, Yuli Lyanda-Geller, and Leonid P Rokhinson. Evidence for reversible control of magnetization in a ferromagnetic material by means of spin-orbit magnetic field. Nat. Phys., 5(9):656–659, 2009.
- [9] Luqiao Liu, Chi Feng Pai, Y Li, HW Tseng, DC Ralph, and RA Buhrman. Spin-torque switching with the giant spin hall effect of tantalum. Sci., 336(6081):555–558, 2012.
- [10] Arne Brataas and Kjetil Hals. Spin-orbit torques in action. Nat. Nanotechnol., 9(2):86–88, 2014.
- [11] Murat Cubukcu, Olivier Boulle, Marc Drouard, Kevin Garello, Can Onur Avci, Ioan Mihai Miron, Juergen Langer, Berthold Ocker, Pietro Gambardella, and Gilles Gaudin. Spin-orbit torque magnetization switching of a three-terminal perpendicular magnetic tunnel junction. Appl. Phys. Lett., 104(4):042406, 2014.
- [12] JE Hirsch. Spin hall effect. Phys. Rev. Lett., 83(9):1834, 1999.
- [13] Saburo Takahashi and Sadamichi Maekawa. Spin current, spin accumulation and spin hall effect. Sci. Technol. Adv. Mater., 9(1):014105, 2008.
- [14] D A Pesin and A H MacDonald. Quantum kinetic theory of current-induced torques in rashba ferromagnets. Phys. Rev. B, 86(1):014416, 2012.

- 
- [15] Kotb Jabeur, Gregory Di Pendina, Fabrice Bernard-Granger, and Guillaume Prenat. Spin orbit torque non-volatile flip-flop for high speed and low energy applications. IEEE Electron Device Lett., 35(3):408–410, 2014.
- [16] Guillaume Prenat, Kotb Jabeur, Pierre Vanhauwaert, Gregory Di Pendina, Fabian Oboril, Rajendra Bishnoi, Mojtaba Ebrahimi, Nathalie Lamard, Olivier Boule, Kevin Garello, et al. Ultra-fast and high-reliability sot-mram: From cache replacement to normally-off computing. IEEE Trans. Multi-Scale Comput. Syst., 2(1):49–60, 2015.
- [17] Sabpreet Bhatti, Rachid Sbiaa, Atsufumi Hirohata, Hideo Ohno, Shunsuke Fukami, and SN Piramanayagam. Spintronics based random access memory: a review. Mater. Today, 20(9):530–548, 2017.
- [18] Masahiko Nakayama, Tadashi Kai, Naoharu Shimomura, Minoru Amano, Eiji Kitagawa, Toshihiko Nagase, Masatoshi Yoshikawa, Tatsuya Kishi, Sumio Ikegawa, and Hiroaki Yoda. Spin transfer switching in tb co fe/ co fe b/ mg o/ co fe b/ tb co fe magnetic tunnel junctions with perpendicular magnetic anisotropy. J. Appl. Phys., 103(7):07A710, 2008.
- [19] S Ikeda, K Miura, H Yamamoto, K Mizunuma, HD Gan, M Endo, Sl Kanai, J Hayakawa, F Matsukura, and H Ohno. A perpendicular-anisotropy cofeb–mgo magnetic tunnel junction. Nat. Mater., 9(9):721–724, 2010.
- [20] S-W Chung, Tatsuya Kishi, Jung Woo Park, Masatoshi Yoshikawa, Kyung-Seok Park, Toshihiko Nagase, K Sunouchi, H Kanaya, GC Kim, K Noma, et al. 4gbt density stt-mram using perpendicular mtj realized with compact cell structure. In

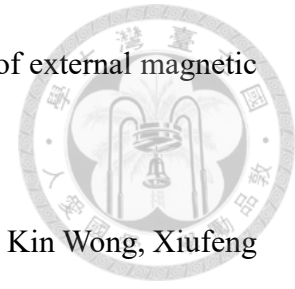
2016 IEEE International Electron Devices Meeting (IEDM), pages 27.1.1–27.1.4.  
IEEE, 2016.



- [21] Luqiao Liu, OJ Lee, TJ Gudmundsen, DC Ralph, and RA Buhrman. Current-induced switching of perpendicularly magnetized magnetic layers using spin torque from the spin hall effect. Phys. Rev. Lett., 109(9):096602, 2012.
- [22] Meiyin Yang, Kaiming Cai, Hailang Ju, Kevin William Edmonds, Guang Yang, Shuai Liu, Baohe Li, Bao Zhang, Yu Sheng, Shouguo Wang, et al. Spin-orbit torque in pt/conico/pt symmetric devices. Sci. Rep., 6(1):20778, 2016.
- [23] Shouzhong Peng, Daoqian Zhu, Jiaqi Zhou, Boyu Zhang, Anni Cao, Mengxing Wang, Wenlong Cai, Kaihua Cao, and Weisheng Zhao. Modulation of heavy metal/ferromagnetic metal interface for high-performance spintronic devices. Adv. Electron. Mater., 5(8):1900134, 2019.
- [24] Hao Wu, Jing Zhang, Baoshan Cui, Seyed Armin Razavi, Xiaoyu Che, Qunjun Pan, Di Wu, Guoqiang Yu, Xiufeng Han, and Kang L Wang. Field-free approaches for deterministic spin-orbit torque switching of the perpendicular magnet. Mater. Futures, 1:022201, 2022.
- [25] Yong Chang Lau, Davide Betto, Karsten Rode, JMD Coey, and Plamen Stamenov. Spin-orbit torque switching without an external field using interlayer exchange coupling. Nat. Nanotechnol., 11(9):758–762, 2016.
- [26] Shunsuke Fukami, Chaoliang Zhang, Samik DuttaGupta, Aleksandr Kurenkov, and Hideo Ohno. Magnetization switching by spin-orbit torque in an antiferromagnet-ferromagnet bilayer system. Nat. Mater., 15(5):535–541, 2016.

- 
- [27] Long You, OukJae Lee, Debanjan Bhowmik, Dominic Labanowski, Jeongmin Hong, Jeffrey Bokor, and Sayeef Salahuddin. Switching of perpendicularly polarized nano-magnets with spin orbit torque without an external magnetic field by engineering a tilted anisotropy. PNAS, 112(33):10310–10315, 2015.
- [28] Fengmao Wang, Xiangli Zhang, Zongzhi Zhang, and Yaowen Liu. Deterministic magnetization switching by spin–orbit torque in a ferromagnet with tilted magnetic anisotropy: A macrospin modeling. J. Magn. Magn. Mater., 527:167757, 2021.
- [29] Behzad Zeinali, Jens K Madsen, Praveen Raghavan, and Farshad Moradi. Ultra-fast sot-mram cell with stt current for deterministic switching. In 2017 IEEE International Conference on Computer Design (ICCD), pages 463–468. IEEE, 2017.
- [30] Mengxing Wang, Wenlong Cai, Daoqian Zhu, Zhaohao Wang, Jimmy Kan, Zhengyang Zhao, Kaihua Cao, Zilu Wang, Youguang Zhang, Tianrui Zhang, et al. Field-free switching of a perpendicular magnetic tunnel junction through the interplay of spin–orbit and spin-transfer torques. Nat. Electron., 1(11):582–588, 2018.
- [31] Sachin Pathak, Chanyoung Youm, and Jongill Hong. Impact of spin-orbit torque on spin-transfer torque switching in magnetic tunnel junctions. Sci. Rep., 10(1):2799, 2020.
- [32] Andrea Meo, Jessada Chureemart, Roy W Chantrell, and Phanwadee Chureemart. Magnetisation switching dynamics induced by combination of spin transfer torque and spin orbit torque. Sci. Rep., 12(1):3380, 2022.
- [33] Guoqiang Yu, Pramey Upadhyaya, Yabin Fan, Juan G Alzate, Wanjun Jiang, Kin L Wong, So Takei, Scott A Bender, Li Te Chang, Ying Jiang, et al. Switching of per-

pendicular magnetization by spin–orbit torques in the absence of external magnetic fields. Nat. Nanotechnol., 9(7):548–554, 2014.



[34] Armin Razavi, Hao Wu, Qiming Shao, Chi Fang, Bingqian Dai, Kin Wong, Xiufeng Han, Guoqiang Yu, and Kang L Wang. Deterministic spin–orbit torque switching by a light-metal insertion. Nano letters, 20(5):3703–3709, 2020.


[35] Armin Razavi, Hao Wu, Bingqian Dai, Haoran He, Di Wu, Kin Wong, Guoqiang Yu, and Kang L Wang. Spin–orbit torques in structures with asymmetric damping layers. Applied Physics Letters, 117(18):182403, 2020.

[36] Baoshan Cui, Hao Wu, Dong Li, Seyed Armin Razavi, Di Wu, Kin L Wong, Meixia Chang, Meizhen Gao, Yalu Zuo, Li Xi, et al. Field-free spin–orbit torque switching of perpendicular magnetization by the rashba interface. ACS applied materials & interfaces, 11(42):39369–39375, 2019.

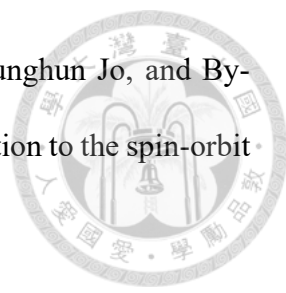
[37] Guoqiang Yu, Li-Te Chang, Mustafa Akyol, Pramey Upadhyaya, Congli He, Xiang Li, Kin L Wong, Pedram Khalili Amiri, and Kang L Wang. Current-driven perpendicular magnetization switching in ta/cofeb/[taox or mgo/taox] films with lateral structural asymmetry. Applied Physics Letters, 105(10):102411, 2014.

[38] Kaiming Cai, Meiyin Yang, Hailang Ju, Sumei Wang, Yang Ji, Baohe Li, Kevin William Edmonds, Yu Sheng, Bao Zhang, Nan Zhang, et al. Electric field control of deterministic current-induced magnetization switching in a hybrid ferromagnetic/ferroelectric structure. Nat. Mater., 16(7):712–716, 2017.

[39] Meiyin Yang, Yongcheng Deng, Kaiming Cai, Hailang Ju, Shuai Liu, Baohe Li, and Kaiyou Wang. Deterministic magnetic switching of perpendicular magnets by gradient current density. J. Magn. Magn. Mater., 489:165474, 2019.

- 
- [40] Shaohai Chen, Jihang Yu, Qidong Xie, Xiangli Zhang, Weinan Lin, Liang Liu, Jing Zhou, Xinyu Shu, Rui Guo, Zongzhi Zhang, et al. Free field electric switching of perpendicularly magnetized thin film by spin current gradient. ACS Appl. Mater. Interfaces, 11(33):30446–30452, 2019.
- [41] Claas Abert, Michele Ruggeri, Florian Bruckner, Christoph Vogler, Gino Hrkac, Dirk Praetorius, and Dieter Suess. A three-dimensional spin-diffusion model for micromagnetics. Sci. Rep., 5(1):14855, 2015.
- [42] Serban Lepadatu. Unified treatment of spin torques using a coupled magnetisation dynamics and three-dimensional spin current solver. Sci. Rep., 7(1):12937, 2017.
- [43] Claas Abert. Micromagnetics and spintronics: models and numerical methods. Eur. Phys. J. B, 92(6):120, 2019.
- [44] Serban Lepadatu. Boris computational spintronics—high performance multi-mesh magnetic and spin transport modeling software. J. Appl. Phys., 128(24):243902, 2020.
- [45] Serban Lepadatu. Effect of inter-layer spin diffusion on skyrmion motion in magnetic multilayers. Sci. Rep., 9(1):9592, 2019.
- [46] Callum Robert MacKinnon, Serban Lepadatu, Tim Mercer, and Philip Raymond Bissell. Role of an additional interfacial spin-transfer torque for current-driven skyrmion dynamics in chiral magnetic layers. Phys. Rev. B, 102(21):214408, 2020.
- [47] Callum R MacKinnon, Katharina Zeissler, Simone Finizio, Jörg Raabe, Christopher H Marrows, Tim Mercer, Philip R Bissell, and Serban Lepadatu. Collective skyrmion motion under the influence of an additional interfacial spin-transfer torque. Sci. Rep., 12(1):10786, 2022.



- 
- [48] Soonha Cho, Seung heon Chris Baek, Kyeong Dong Lee, Younghun Jo, and Byong Guk Park. Large spin hall magnetoresistance and its correlation to the spin-orbit torque in w/cofeb/mgo structures. Sci. Rep., 5(1):14668, 2015.
- [49] Yutaro Takeuchi, Chaoliang Zhang, Atsushi Okada, Hideo Sato, Shunsuke Fukami, and Hideo Ohno. Spin-orbit torques in high-resistivity-w/cofeb/mgo. Appl. Phys. Lett., 112(19):192408, 2018.
- [50] Shinji Isogami, Yohei Shiokawa, Atsushi Tsumita, Eiji Komura, Yugo Ishitani, Kosuke Hamanaka, Tomohiro Taniguchi, Seiji Mitani, Tomoyuki Sasaki, and Masamitsu Hayashi. Spin-orbit torque driven magnetization switching in w/cofeb/mgo-based type-y three terminal magnetic tunnel junctions. Sci. Rep., 11(1):16676, 2021.
- [51] RL de Orio, A Makarov, S Selberherr, W Goes, J Ender, S Fiorentini, and V Sverdlov. Robust magnetic field-free switching of a perpendicularly magnetized free layer for sot-mram. Solid-State Electronics, 168:107730, 2020.
- [52] Stanislaw Halas and Tomasz Durakiewicz. Work functions of elements expressed in terms of the fermi energy and the density of free electrons. J. Phys.: Condens. Matter, 10(48):10815, 1998.
- [53] S X Huang, T Y Chen, and C L Chien. Spin polarization of amorphous cofeb determined by point-contact andreev reflection. Appl. Phys. Lett., 92(24):242509, 2008.
- [54] Chi Feng Pai, Luqiao Liu, Y Li, HW Tseng, DC Ralph, and RA Buhrman. Spin transfer torque devices utilizing the giant spin hall effect of tungsten. Appl. Phys. Lett., 101(12):122404, 2012.